Received: 12 November 2021 | Revised: 9 February 2022 | Accepted: 27 March 2022

DOI: 10.1002/aic.17704

AIChE JOURNAL

RESEARCH ARTICLE

Transport Phenomena and Fluid Mechanics

Drop breakup and entrainment in the updraft

Hai-Feng Liu | Yu-Fan Wang | Hui Zhao | Wei-Feng Li | Jian-Liang Xu

Shanghai Engineering Research Center of Coal Gasification, East China University of Science and Technology, Shanghai 200237, China

Correspondence
Hui Zhao, Shanghai Engineering Research Center of Coal Gasification, East China University of Science and Technology, Shanghai 200237, China.
Email: zhaohui@ecust.edu.cn

Funding information
Fundamental Research Funds for the Central Universities; National Natural Science Foundation of China, Grant/Award Number: U21B2088

Abstract

This study aims to investigate the characteristics of gas–liquid countercurrent contact processes. In spray towers or other applications, several drops containing pollutants are entrained by the updraft flue gas, which can easily cause environmental pollution. Traditionally, this drop entrainment phenomenon is alleviated by increasing the diameter of the drops. However, the breakup of a large drop would also cause drop entrainment to become serious, a process referred to as secondary atomization. Herein, we propose the boundary of three drop modes in the updraft: drop falling mode, reverse entrainment mode, and breakup entrainment mode. The critical Weber number (*We*) is the key dimensionless number marking the beginning of the drop breakup. The ratio of the drag force to gravity and *We* are proposed as criteria for the drop entrainment.

KEYWORDS
drop breakup, entrainment, gas–liquid countercurrent, secondary atomization

1 | INTRODUCTION

The motion and breakup of drops are common in daily life and engineering applications.[1–5] Raindrops grow and then fall by accretion of vapor and coalescence inside the clouds. The largest recorded raindrop diameter was 8.8–10 mm, measured at the base of a cumulus congestus cloud in the vicinity of Kwajalein Atoll in July 1999 and over northern Brazil in September 1995.[6,7] The maximum dimension of raindrops at ground level is approximately 4–6 mm.[8–10] Raindrops result from a complex mutual interaction between air and its neighbors. The free-fall of a large raindrop in a gaseous phase can occur in several stages: destabilization, deformation, and ultimate fragmentation. When the spherical drop encounters the gas flow, aerodynamic forces cause the drop to deform and break apart into fragments, a process referred to as secondary atomization.[11–18] The Weber number (*We*) is an essential dimensionless parameter that represents the ratio of disruptive hydrodynamic forces to the stabilizing surface tension force.

$$We = \frac{\rho_g u^2 D_0}{\sigma}, \tag{1}$$

where ρ_g is the ambient gas density, u is the relative velocity between the gas and drop, D_0 is the initial diameter of a liquid drop, and σ is the surface tension.

In many engineering applications, drop behavior also plays an important role. Wet flue-gas desulfurization is a gas–liquid two-phase reaction with high desulfurization efficiency, high reaction speed, and high utilization rate of desulfurization additives; as a result, it is widely used in coal-fired power plants and other factories.[19–21] Although the application of this technology has greatly reduced the concentration of exhaust smoke pollutants, the entrainment of drops also leads to a series of new problems, such as gypsum rain and acid rain that pollute the power plant and surrounding environment, while also corroding equipment.[22,23] The spray tower is the core equipment in the wet flue-gas desulfurization process of a coal-fired power plant boiler tail gas.[24–26] In the spray tower, the limestone slurry washes the flue gas, essentially a gas–liquid two-phase countercurrent contact process, and a gas–liquid mass transfer is accompanied by a two-phase flow process. During the gas–liquid two-phase countercurrent contact process, drops will continue to leave the spray layer under the action of the flue gas and enter the mist eliminator for gas–liquid separation. The upward process of the drops carried by the flue gas is the continuation of the desulfurization reaction. The size of the drops determines the gas–liquid two-phase mass transfer reaction rate

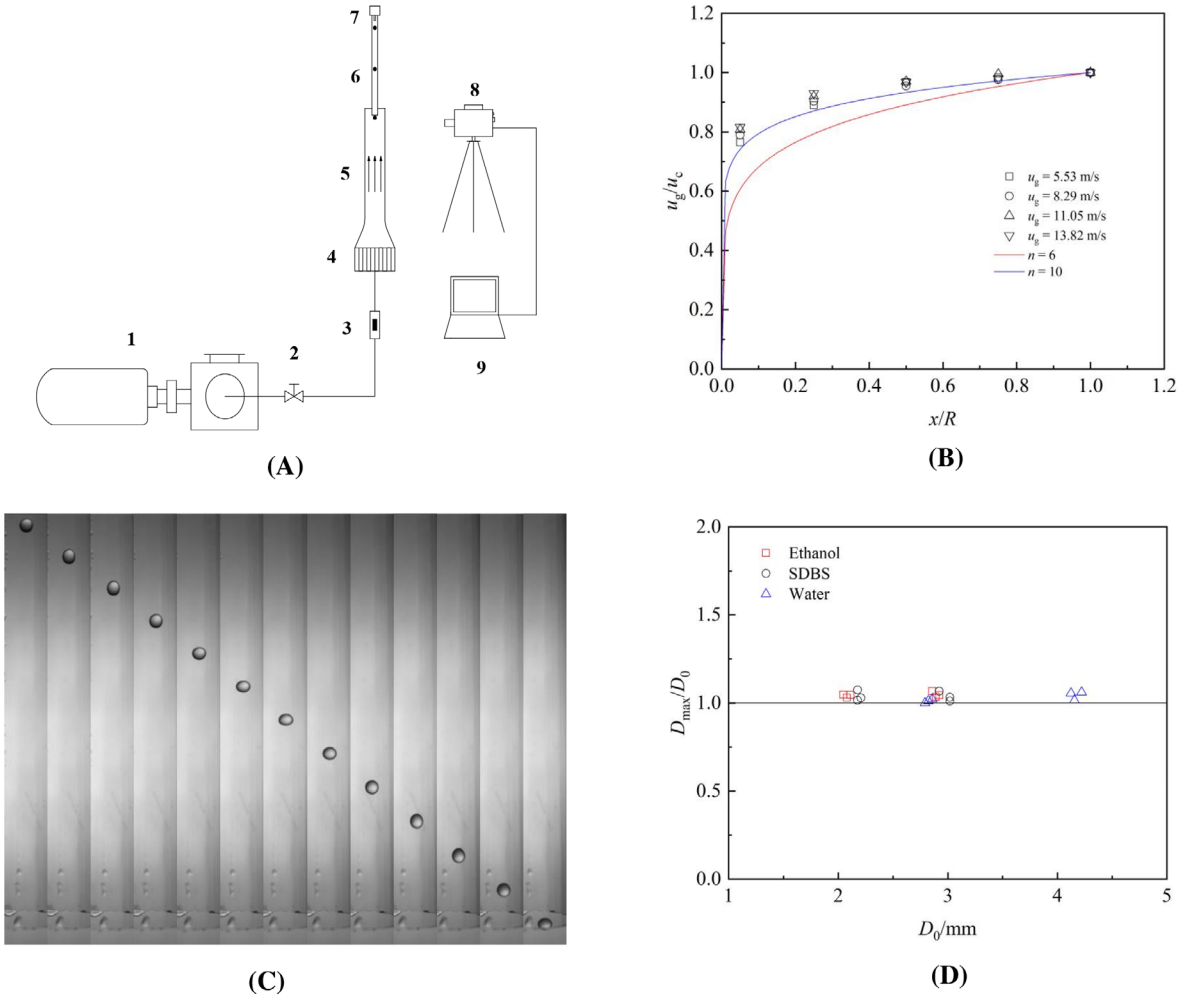

FIGURE 1 Experimental device for the drop entrainment. (A) Experiment sketch of the drop test: 1, air blower; 2, valve; 3, flowmeter; 4, honeycomb plate; 5, drop test section; 6, tube; 7, drop generator; 8, high-speed camera; 9, computer. (B) Gas velocity distribution at the outlet of the pipe. (C) Drop oscillation in the absence of an external air flow. (D) Deformation degree of the drops in the absence of an external air flow

and provides a design basis for the manufacture of gas–liquid separation demisters. Therefore, for spray towers, research on internal gas–liquid countercurrent contact, drop breakup, and entrainment processes are particularly important.[27–29]

In this study, the behaviors of drops in the updraft under different conditions were first observed using a high-speed camera; the characteristics of the drop breakup and entrainment were investigated. Then, a modified map of dimensionless numbers on the drop entrainment relationship was proposed. Three modes of drops in the updraft and corresponding theoretical range were studied. We investigated the characteristics of the surfactant solution drop to test the effect of the dynamic surface tension.

2 | EXPERIMENTAL SETUP

The experimental device for the drop test is shown in Figure 1. The air flow generated by the air blower passed through the honeycomb plate and entered the test section. Drops were formed on the nozzle of the drop generator and fell through the tube in quiescent air before entering the test section. In this test, the range of the drop diameter was between 1.4 and 4.2 mm, and the range of the corresponding drop volume was 1.4–38.8 mm^3. The drop diameter changed by the exchangeable small-diameter tube exit, consistent with our previous work.[30–32] The drop generator, including a cylinder liquid chamber and an exchangeable small-diameter tube, was fixed at the bottom of the water chamber. Liquid drops dripped from the tip of the tube under the action of gravity and fell into the test section. The internal radius R of the drop test section (part 5), as shown in Figure 1A, was 40 mm, and the length H from the honeycomb plate to drop test section was approximately 800 mm. The measured air velocity profile of the drop test section is shown in Figure 1B, almost similar to the classic power-law profile given by $u_g/u_c = (x/R)^{1/n}$, where u_c is the centerline mean velocity of the drop test section, and x is the horizontal distance from the measuring point to the wall of the drop test section. The velocity profiles remained constant at different air velocities. The influence of wall effects on the motion of a falling drop has attracted considerable attention[33–37] because it may result in a larger fluid friction force on the sphere, whose velocity is

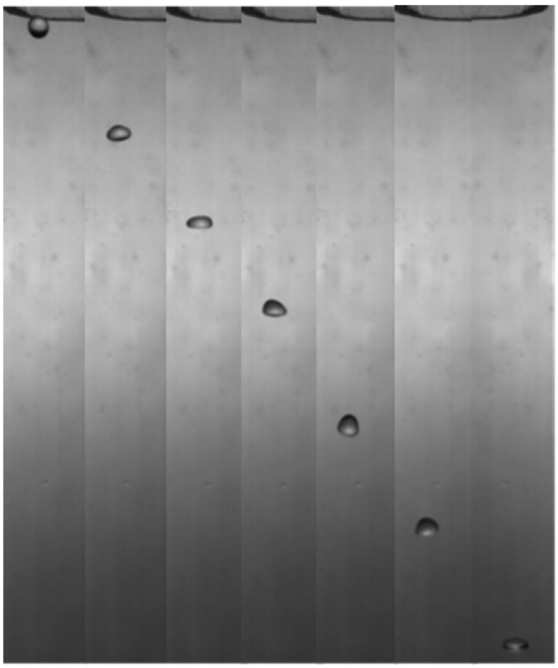

FIGURE 2 Drop falling mode

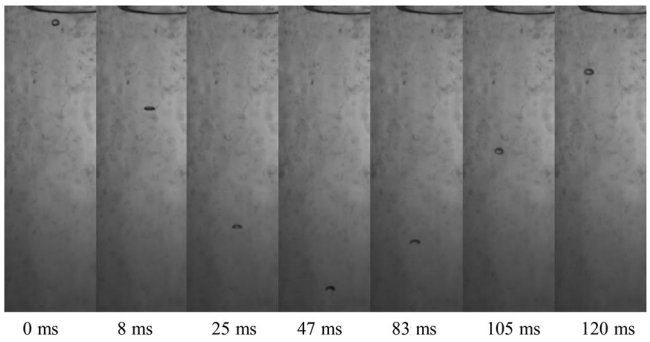

FIGURE 3 Drop reverse entrainment mode

known to be reduced, especially when the sphere is very close to the wall. The internal radius R_1 of the tube (part 6 in Figure 1A) was 12 mm. The tube diameter was relatively large compared to the droplet diameter; therefore, wall effects were not significant. Simultaneously, the velocity of the falling drop at the tube exit (part 6 in Figure 1A) was measured using the image method.

A high-speed camera (Fastcam SA2 by Photron Limited) recorded the entire process of drop deformation and breakup. The experimental liquid included water, alcohol, and surfactant solutions (sodium dodecylbenzene sulfonate solution, SDBS). A dynamic surface tensiometer (SITA science line t100, SITA Messtechnik GmbH, Germany) was used to measure the dynamic surface tension of the surfactant solutions according to the bubble pressure method. The air velocity in the test section was 2.8–13.8 m/s, and the Reynolds number *Re* of

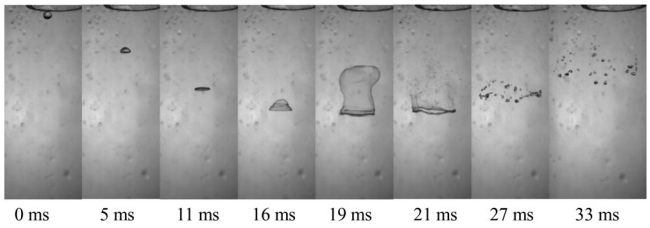

FIGURE 4 Drop-breakup entrainment mode

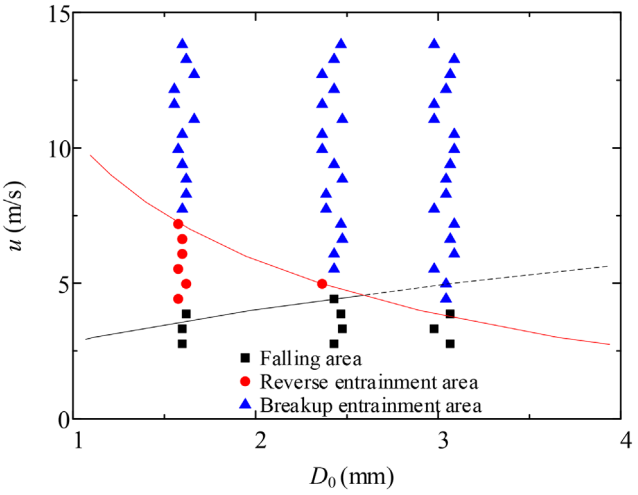

FIGURE 5 Three modes of drop behavior in the updraft under different conditions (alcohol)

the air flow ranged from 1.6×10^4 to 7.9×10^4. The drop Weber number *We* ranged from 1.2 to 52.4.

The falling drop at the tube (part 6 in Figure 1A) in the absence of an external air flow oscillated slightly, as shown in Figure 1C. The results of the oscillation drops with different properties are shown in Figure 1D. Here, D_0 is the initial diameter of the liquid drop, and D_{max} is the maximum cross-flow diameter of the oscillation drop. We found that D_{max} was slightly larger than D_0 in the absence of external air flow.

For the pure liquid, the falling drop undergoes internal circulation flow due to the interaction of the gas–liquid interface. For the surfactant solution, the motion of the liquid caused an uneven distribution of the surfactant on the interface, possibly leading to surface tension gradients. The surfactant exchange caused the surface tension to vary locally, thus, generating Marangoni stresses and convections. The Marangoni effect is the tendency for the mass to travel to areas of higher surface tension within a liquid, hindering the internal circulation flow of the falling drop. When the falling drops oscillated under the condition of a large drop in the Reynolds number, the situation became more complicated. The oscillation of the drop was the main motion resistance, and the effect of the surfactant decreases gradually.[38–45]

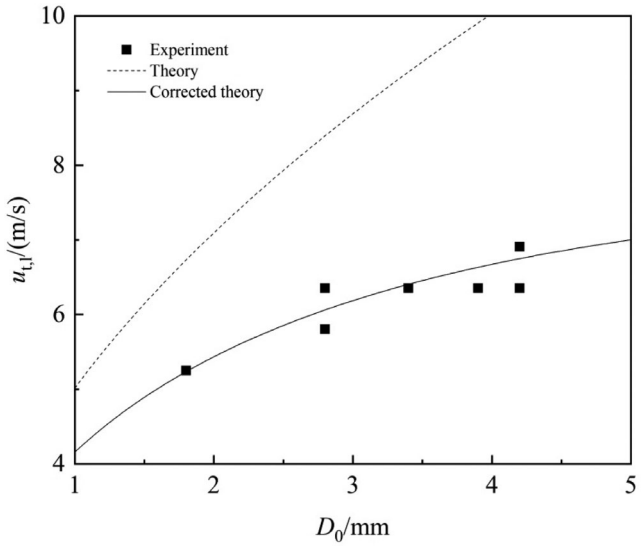

FIGURE 6 Comparison of the actual measurement and theory on terminal velocity of the drop

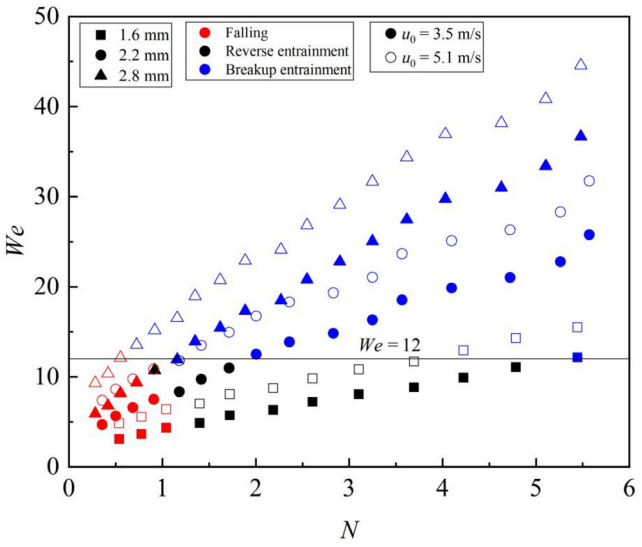

FIGURE 8 Relationship diagram of the drop entrainment, no corrected *N*, alcohol

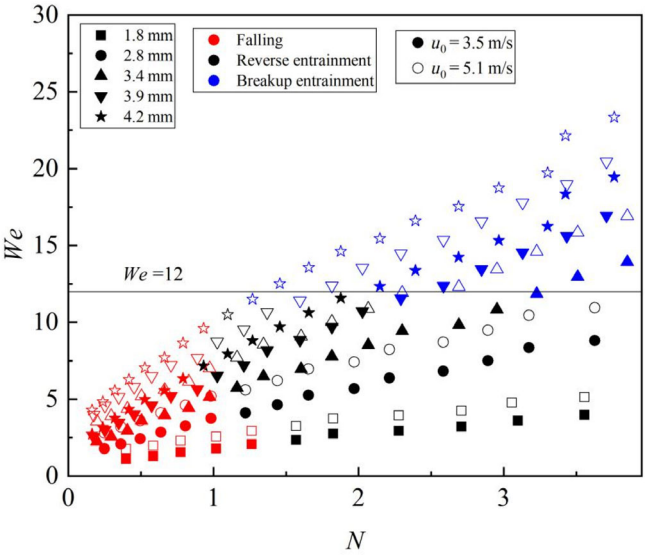

FIGURE 7 Relationship diagram of the drop entrainment, no corrected *N*, water

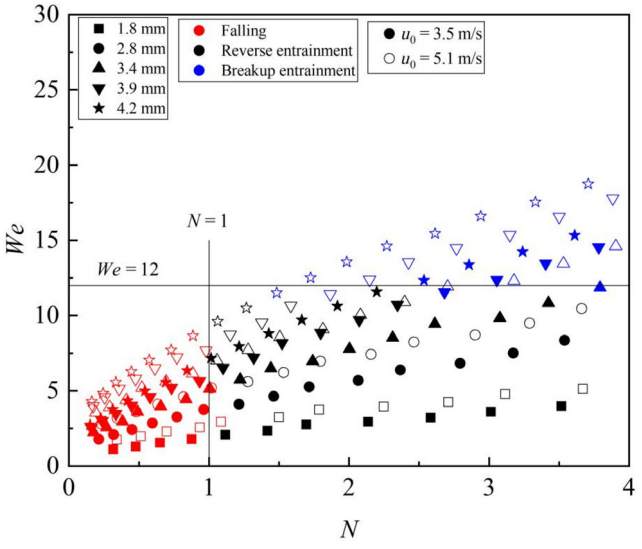

FIGURE 9 Relationship diagram of the drop entrainment, corrected *N*, water

3 | RESULTS AND DISCUSSION

3.1 | Three modes of drops in the updraft

During the experiment, the air flow continuously exerts a force on the drop. As a result, the drop deforms in the air flow, and the behavior trajectory changes. In this experiment, the drop behavior is divided into three modes: drop-falling mode, reverse entrainment mode, and breakup entrainment mode, as shown in Figures 2–4. To describe the behavioral characteristics of the drop, we consider the moment when the drop entered the updraft as the initial time ($t = 0$ ms) and obtain the time series diagram of the drop through a high-speed camera. In the drop falling mode, owing to the weak aerodynamic force, the gas flow only causes the drop to oscillate and deform rather than to break or entrainment, as shown in Figure 2. It can be seen from the pictures that when the drop just enters the gas flow, the drop still maintains a spherical shape, and then deforms under the action of the gas flow. Finally, due to gravity, the drop falls.

In the drop reverse entrainment mode, the air flow gradually slows down the drop, and the aerodynamic forces decrease by competing with gravity. In this process, the drop oscillates and deforms rather than breaking, as shown in Figure 3. At $t = 47$ ms, the drop is at the critical point of falling and then moves upward with the gas flow. At this time, the drop undoubtedly features a disk-like shape.

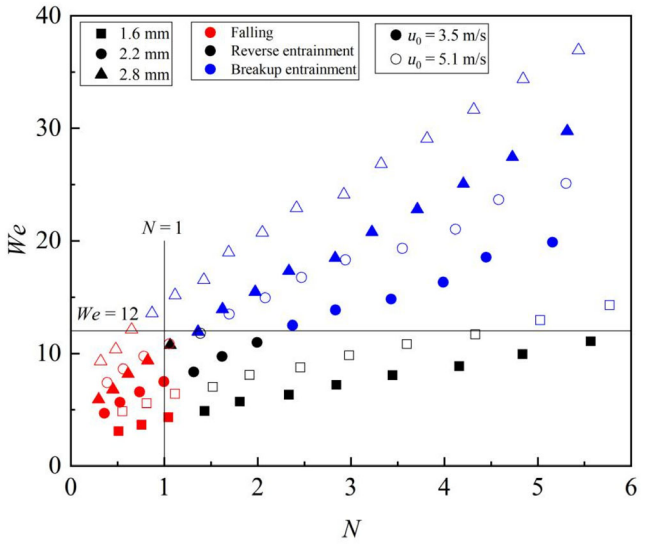

FIGURE 10 Relationship diagram of the drop entrainment, corrected *N*, alcohol

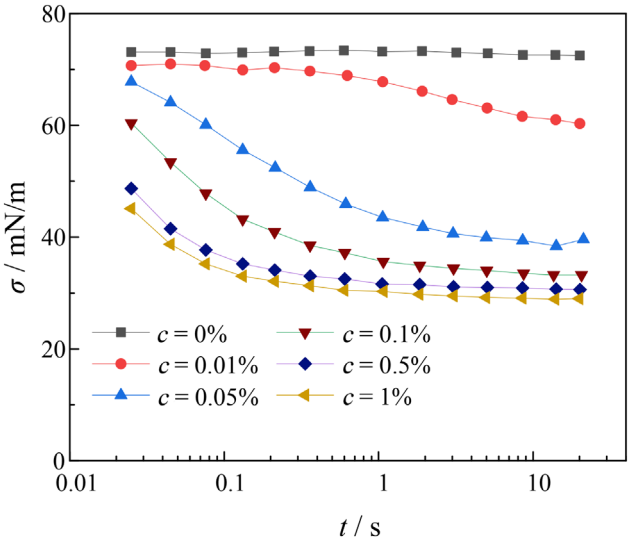

FIGURE 11 Dynamic surface tension of surfactant solutions

In the drop-breakup entrainment mode, the aerodynamic force is sufficiently large to cause the drop to break against the surface tension. As shown in Figure 4, the drop gradually deforms and transforms into two parts—ring- and bag-like shapes—along the direction of the air flow. The bag-like part breaks first, and the diameter of the fragment is considerably small. The ring part subsequently breaks up, and the corresponding fragment has a larger diameter than the bag-like part. As the size of the broken fragments are very small, they are all entrained with the rising gas flow.

As shown in Figure 5, drop behavior in the updraft is divided into three modes under different conditions. We find that with an increase in the drop diameter, the drop falls at a higher gas velocity, implying the area of the drop-falling mode increases gradually. However, due to the drop breakup at a high gas velocity (or *We*), when the drop diameter is bigger than approximately 2.5 mm, the drop-breakup entrainment mode plays an important role. Then, with an increase in the drop diameter, the area of the drop-falling mode decreases gradually.

3.2 | Force analysis of drops

In this experiment, the surface tension prevents the drop from breaking. The other two main forces—gravity and aerodynamic force—control the motion behavior of the drop. According to the aerodynamic formula of the drop,

$$F=\frac{1}{2}C_D\rho_g S u_g^2, \tag{2}$$

where C_D is the drag coefficient, S is the windward area of the drop, and u_g is the gas velocity. From Equation (2) it follows:

$$F=\frac{1}{8}\pi C_D\rho_g D_0^2 u_g^2, \tag{3}$$

where D_0 is the initial diameter of the drop. The ratio of the drop gravity to the aerodynamic force is

$$\frac{F}{G}=\frac{\frac{1}{8}\pi C_D\rho_g D_0^2 u_g^2}{\frac{4}{3}\pi\rho_l\frac{D_0^3}{8}g}=\frac{3C_D\rho_g u_g^2}{4\rho_l g D_0}, \tag{4}$$

where ρ_l is the density of the liquid phase, and g is the acceleration of gravity. To facilitate the analysis, we propose a dimensionless number N describing preliminarily the entrainment of the drop:

$$N=\frac{3C_D\rho_g u_g^2}{4\rho_l g D_0}. \tag{5}$$

Liu et al.[46] discovered that C_D is a function of deformation, which is defined as

$$C_D/C_S=1+2.632\left[1-(D_0/D_{max})^2\right], \tag{6}$$

where C_S is the drag coefficient of the drop under the same *Re* and C_S, which is 0.44. D_{max} is the maximum cross-flow diameter of the drop in the airflow, and Hsiang and Faeth[47] found that

$$\frac{D_{max}}{D_0}=1+0.19We^{0.5}. \tag{7}$$

Thus, by using Equations (6) and (7), C_D of the drop in the gas flow can be obtained.

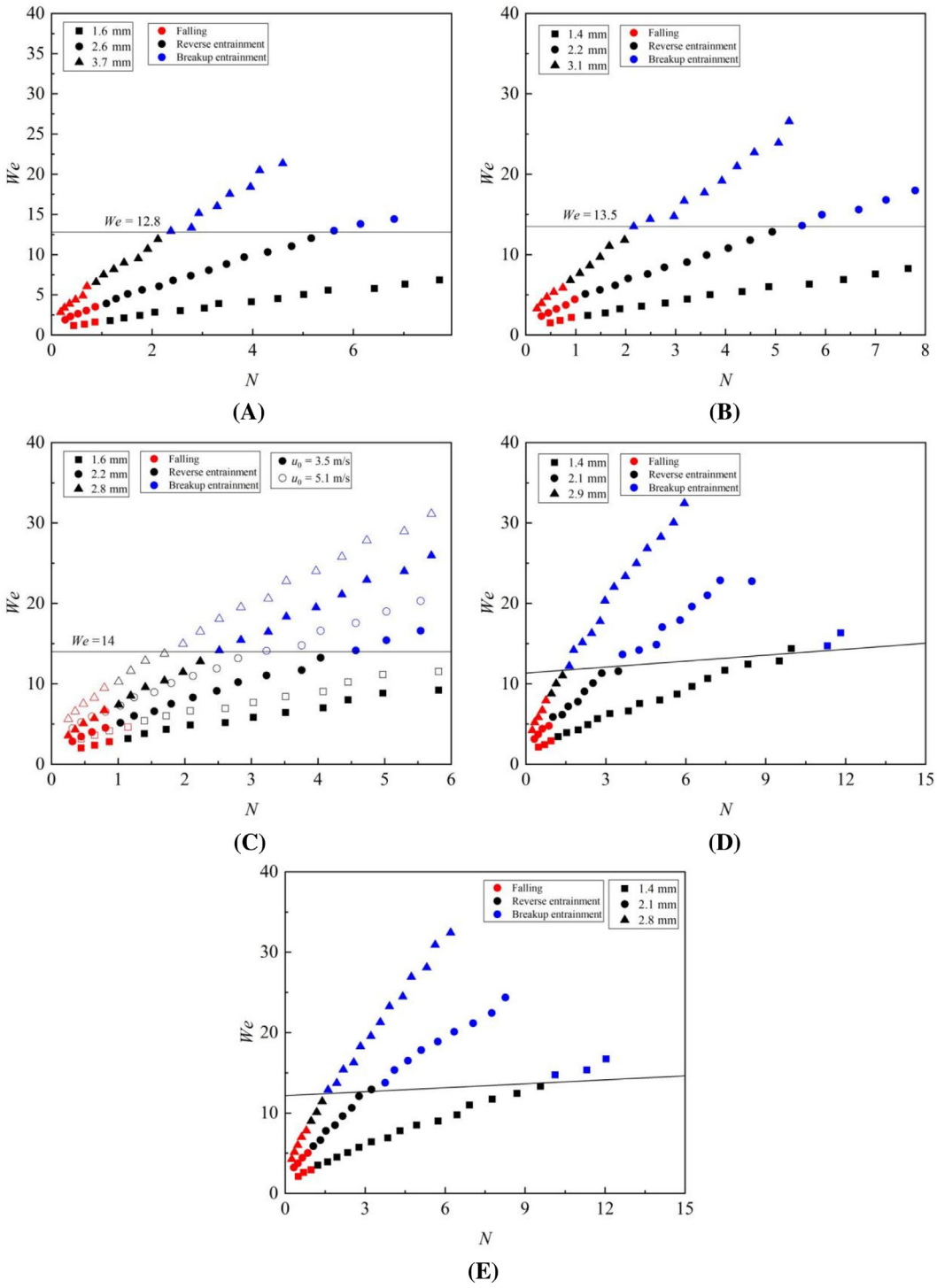

FIGURE 12 Sodium dodecylbenzene sulfonate solution drop entrainment diagram, no corrected *N*. (A) 0.01 wt%; (B) 0.05 wt%; (C) 0.1 wt%; (D) 0.5 wt%; (E) 1 wt%

3.3 | Falling velocity of the drop

In the experiments, the falling velocities of drops of different diameters in the air flow are denoted with $u_{t,l}$. According to the force balance between the drop gravity and aerodynamic force, the terminal velocity formula of the ideal spherical drops is calculated as follows:

$$u_{t,l} = 1.74\sqrt{\frac{D_0\rho_l g}{\rho_g}}. \tag{8}$$

This value is also very similar to the literature report.[48,49] It is observed experimentally that the drop deforms in the air flow, increasing its windward area increases, resulting in a corresponding increase in the

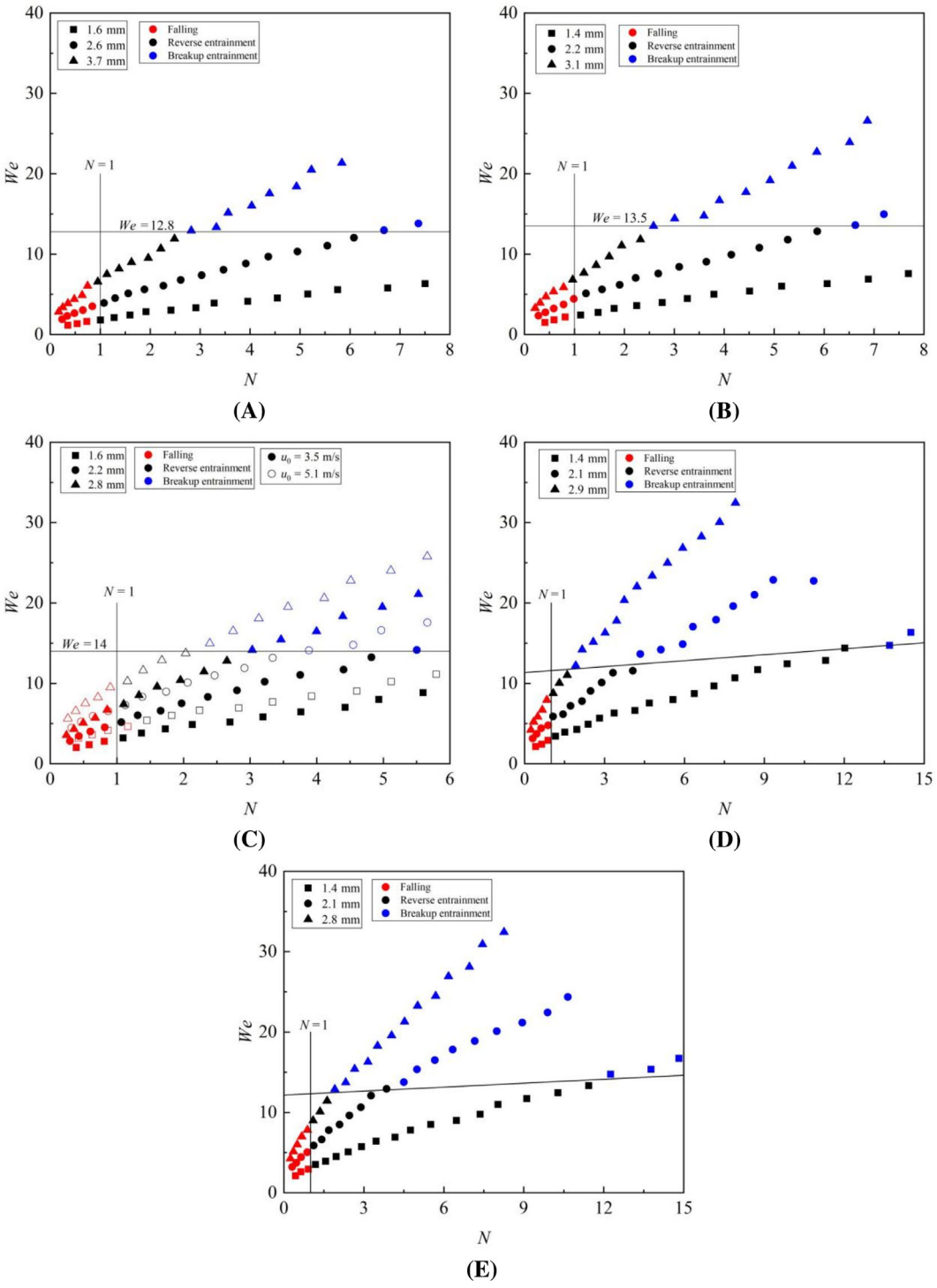

FIGURE 13 Sodium dodecylbenzene sulfonate solution drop entrainment diagram, corrected *N*. (A) 0.01 wt%; (B) 0.05 wt%; (C) 0.1 wt%; (D) 0.5 wt%; (E) 1 wt%

aerodynamic force on the drop; therefore, the measured drop terminal velocity is smaller than the theoretical value used in Equation (8). The drop deformation in Equation (7) is introduced to modify the theoretical velocity of the drops to eliminate this difference. Therefore, we finally obtain the formula for the terminal velocity of the drop in the updraft:

$$u'_{t,l} = \frac{1.74}{1+0.19We^{0.5}}\sqrt{\frac{D_0\rho_l g}{\rho_g}}. \quad (9)$$

The experimental, theoretical, and corrected theoretical values are shown in Figure 6. After the correction, the theoretical and experimental values exhibit a better fitting relationship.

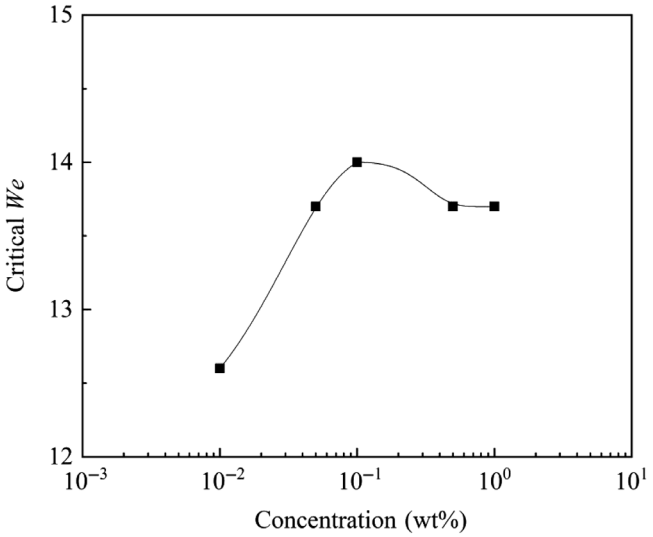

FIGURE 14 Critical *We* at different sodium dodecylbenzene sulfonate solution concentrations

3.4 | Analysis of the drop breakup and entrainment

The relationship between the *We* and *N* values under different conditions is discussed to further determine the basis for the occurrence of reverse and breakup entrainments. Instead of using C_D to correct *N*, we try using a simpler *N* value to study the entrainment, as shown in Figures 7 and 8. Here, u_0 is the initial velocity of the drop when it is just beginning to come into contact with the updraft.

In the above figures, *N* is the ratio of the aerodynamic force and gravity without C_D correction; the critical conditions of entrainment are distributed around $N = 1$. As the deformation degrees of the drop vary under different conditions, the drag coefficient C_D is a variable. In addition to the attempt above, we correct *N*, which leads to the data shown in Figures 9 and 10.

After the correction of *N*, an *N* value of 1 can be approximated as the criterion between drop falling and entrainment. This criterion is mutually confirmed with the simplest force model of the drop and is also consistent with life experience. When the aerodynamic force is greater than gravity, the drops are entrained; when the aerodynamic force is less than gravity, the drops fall. In addition, it can be seen from the figures that under different working conditions, $We = 12$ is another criterion when the drops (water and alcohol) break up and are entrained, consistent with the results of the literature on secondary atomization.[12,13] Therefore, based on the relationship between *We* and *N*, we divide the behavior characteristics of drops under different conditions into three areas: the falling area, the reverse entrainment area, and the breakup entrainment area. Here, we preliminarily propose that the boundaries of the different areas are $N = 1$ and $We = 12$. These relationships can be used as a practical reference in life and industry.

3.5 | Fragment behavior after drop breakup

If the drops break up in the updraft, the fragments formed by the breakup will be reversely entrained in the air flow. Zhao et al.[50] found that the average particle size of the fragments generated when the drops were broken was

$$\frac{D_r}{D_0} = \left(4.3 \times 10^{-3}\right)\left(1 + 890Oh^{0.09}\right)We^{0.82}, \quad (10)$$

where D_r is the average fragment size. In this experiment, the largest drop diameter used is 4.2 mm, so D_r amounts to 1.18 mm. Zhao et al.[50] obtained the gamma distribution of the particle size according to the average particle size. We take $D/D_r = 2.2$ to obtain the largest fragment diameter, yielding a *D* value of 2.6 mm. According to the experimental data, a drop with a diameter of 4.2 mm breaks and entrains. The instantaneous parameters are $u_0 = 0$ and $u_g = 8.8$ m/s. The instantaneous *N* value of a drop with a diameter of 2.6 mm is calculated by $N = 2.5$. Therefore, the largest fragment generated when the drop breaks is $N > 1$, that is, all fragments generated are entrained by the air flow.

3.6 | Effect of surface tension

In applications, many of the used fluids are solutions containing various components. Here, surfactant solutions of different concentrations were selected as test liquids, whose dynamic surface tensions are shown in Figure 11. The dynamic surface tension increases upon decreasing bubble lifetime. The horizontal axis *t* is the bubble lifetime, as shown in Figure 11.

If the concentration of the surfactant is above the critical micelle concentration (CMC), micelles form and all additional surfactants added to the system are incorporated into these micelles; therefore, the CMC is an important characteristic. Before reaching the CMC, the surface tension changes strongly with the surfactant concentration. After reaching the CMC, the surface tension changes with a lower slope. Because of the surfactant, the critical *We* is nonlinear at different concentrations of the surfactant, as shown in Figures 12 and 13.

If the surfactant concentration is smaller than the CMC, it is difficult for the surfactant to be added to the rapidly deformed interface in the air flow over time. Therefore, as the concentration of surfactant at the drop interface decreases, the real surface tension increases, thus increasing the aerodynamic force required for the breakup of the drop, and increasing the critical *We*. If the surfactant concentration is higher than the CMC, the micelles can be considered the source term, which could supply the monomers to the drop interface.[36] Therefore, *We* first increases and then decreases with increasing surfactant concentration, as shown in Figure 14. When the critical *We* reaches the turning point the surfactant concentration is found to be close to the CMC.

4 | CONCLUSIONS

In summary, the characteristics of gas–liquid countercurrent contact processes and drop entrainment were investigated. Three different modes of the falling drop in the updraft were studied: drop-falling mode, reverse entrainment mode, and breakup entrainment mode. Although the large-diameter drops can fall in the updraft, they were also prone to breakup and entrainment. Thus, a larger diameter of the drops does not necessarily lead to a better anti-entrainment effect. Furthermore, the theoretical formulas for predicting the boundary condition of the drop behavior were obtained. A dimensionless number *We*–*N* map of falling drop regions was proposed, which helps understanding the phenomena of the drop behavior in the updraft. The criterion of the different modes was found to be the corrected $N = 1$ and $We = 12$. Finally, the effect of the dynamic surface tension on the drop breakup and entrainment was investigated, showing that the critical *We* first increased and then decreased upon increasing surfactant concentration.

ACKNOWLEDGMENT

This research was supported by the National Natural Science Foundation of China (U21B2088) and the Fundamental Research Funds for the Central Universities.

AUTHOR CONTRIBUTIONS

Hai-Feng Liu: Investigation (equal); methodology (equal). **Yu-Fan Wang:** Investigation (equal); methodology (equal). **Hui Zhao:** Investigation (equal); methodology (equal). **Wei-Feng Li:** Resources (equal). **Jian-Liang Xu:** Resources (equal).

DATA AVAILABILITY STATEMENT

Data available on request from the authors.

ORCID

Hui Zhao https://orcid.org/0000-0002-8379-0399

REFERENCES

1. Yan W-C, Davoodi P, Tong YW, Wang C-H. Computational study of core-shell droplet formation in coaxial electrohydrodynamic atomization process. *AIChE J*. 2016;62(12):4259-4276.
2. Danny Raj M, Rengaswamy R. Interacting coalescence avalanches in a 2D droplet assembly. *AIChE J*. 2019;65(3):1111-1118.
3. White AR, Ward T. Surface remobilization of buoyancy-driven surfactant-laden drops at low Reynolds and capillary numbers. *AIChE J*. 2019;65(1):294-304.
4. Tyagi PK, Kumar R, Mondal PK. A review of the state-of-the-art nanofluid spray and jet impingement cooling. *Phys Fluids*. 2020;32(12):121301.
5. Padwal MB, Natan B, Mishra DP. Gel propellants. *Prog Energy Combust*. 2021;83:100885.
6. Beard KV, Johnson DB, Baumgardner D. Aircraft observations of large raindrops in warm, shallow, convective clouds. *Geophys Res Lett*. 1986;13:991-994.
7. Hobbs PV, Rangno AL. Super-large raindrops. *Geophys Res Lett*. 2004;31:405-407.
8. Marshall JS, Palmer WMK. The distribution of raindrops with size. *J Atmos Sci*. 1948;5:165-166.
9. Low TB, List R. Collision, coalescence and breakup of raindrops. Part i: experimentally established coalescence efficiencies and fragment size distributions in breakup. *J Atmos Sci*. 1982;39:1591-1606.
10. Villermaux E, Bossa B. Single-drop fragmentation determines size distribution of raindrops. *Nat Phys*. 2009;5:697-702.
11. Andersson R, Andersson B. Modeling the breakup of fluid particles in turbulent flows. *AIChE J*. 2006;52(6):2031-2038.
12. Guildenbecher DR, López-Rivera C, Sojka PE. Secondary atomization. *Exp Fluids*. 2009;46:371-402.
13. Theofanous TG. Aerobreakup of Newtonian and viscoelastic liquids. *Annu Rev Fluid Mech*. 2011;43:661-690.
14. Meng JC, Colonius T. Numerical simulation of the aerobreakup of a water droplet. *J Fluid Mech*. 2018;835:1108-1135.
15. Kuznetsov GV, Shlegel NE, Solomatin Y, Strizhak PA. Combined techniques of secondary atomization of multi-component droplets. *Chem Eng Sci*. 2019;209:115199.
16. Wang Z, Hopfes T, Giglmaier M, Adams NA. Effect of Mach number on droplet aerobreakup in shear stripping regime. *Exp Fluids*. 2020;61(9):1-17.
17. Dorschner B, Biasiori-Poulanges L, Schmidmayer K, El-Rabii H, Colonius T. On the formation and recurrent shedding of ligaments in droplet aerobreakup. *J Fluid Mech*. 2020;904:A20.
18. Radhakrishna V, Shang W, Yao L, Chen J, Sojka PE. Experimental characterization of secondary atomization at high Ohnesorge numbers. *Int J Multiph Flow*. 2021;138:103591.
19. Jacek M. Development of droplet size distribution in FGD spray towers. *At Sprays*. 2000;10:105-119.
20. Mohan BR, Jain RK, Meikap BC. Comprehensive analysis for prediction of dust removal efficiency using twin-fluid atomization in a spray scrubber. *Sep Purif Technol*. 2008;63(2):269-277.
21. Yang F, Liu H, Feng P, Li Z, Tan H. Effects of wet flue gas desulfurization and wet electrostatic precipitator on particulate matter and sulfur oxide emission in coal-fired power plants. *Energy Fuel*. 2020;34(12):16423-16432.
22. Trompiz CJ, Fair JR. Entrainment from spray distributors for packed columns. *Ind Eng Chem Res*. 2000;39(6):1797-1808.
23. Saushin II, Goltsman AE, Salekhova IG. Drop entrainment in two-phase non concurrent film flow. *J Phys Conf Ser*. 2019;1382:012098.
24. Cui H, Li N, Peng J, Yin R, Li J, Wu Z. Investigation on the thermal performance of a novel spray tower with upward spraying and downward gas flow. *Appl Energy*. 2018;231:12-21.
25. Chen Z, Wang H, Zhuo J, You C. Enhancement of mass transfer between flue gas and slurry in the wet flue gas desulfurization spray tower. *Energy Fuel*. 2018;32(1):703-712.
26. Valera VY, Codolo MC, Martins TD. Artificial neural network for prediction of SO_2 removal and volumetric mass transfer coefficient in spray tower. *Chem Eng Res Des*. 2021;170:1-12.
27. Klee AJ, Treybal RE. Rate of rise or fall of liquid drops. *AIChE J*. 1956;2(4):444-447.
28. Krishna PM, Venkateswarlu D, Narasimhamurty GSR. Fall of liquid drops in water. Drag coefficients, peak velocities, and maximum drop sizes. *J Chem Eng Data*. 1959;4(4):340-343.
29. Volkov RS, Kuznetsov GV, Strizhak PA. Criterion expressions for conditions and deceleration and subsequent entrainment of water drops by high-temperature gases. *Tech Phys*. 2015;60(9):1310-1315.
30. Zhao H, Nguyen D, Duke DJ, et al. Effect of turbulence on drop breakup in counter air flow. *Int J Multiph Flow*. 2019;120:103108.
31. Zhao H, Zhang WB, Xu JL, Li WF, Liu HF. Influence of surfactant on the drop bag breakup in a continuous air jet stream. *Phys Fluids*. 2016;28(5):054102.
32. Zhao H, Liu HF, Li WF, Xu JL. Morphological classification of low viscosity drop bag breakup in a continuous air jet stream. *Phys Fluids*. 2010;22(11):114103.

33. Ambari A, Gauthier-Manuel B, Guyon E. Wall effects on a sphere translating at constant velocity. *J Fluid Mech*. 1984;149:235-253.
34. Machac I, Lecjaks Z. Wall effect for a sphere falling through a non-Newtonian fluid in a rectangular duct. *Chem Eng Sci*. 1995;50(1):143-148.
35. Di Felice R. A relationship for the wall effect on the settling velocity of a sphere at any flow regime. *Int J Multiph Flow*. 1996;22(3):527-533.
36. Ryu S, Matsudaira P. A drag correlation for a nonporous sphere steadily approaching an impermeable plane at finite Reynolds numbers. *Chem Eng Sci*. 2010;65(16):4913-4915.
37. Anderson JD. *Fundamentals of Aerodynamics*. 6th ed. McGraw-Hill Education; 2017.
38. Levich VG. *Physicochemical Hydrodynamics*. Prentice-Hall; 1962.
39. Levich VG, Krylov VS. Surface-tension-driven phenomena. *Annu Rev Fluid Mech*. 1969;1(1):293-316.
40. Harper JF. The motion of bubbles and drops through liquids. *Adv Appl Mech*. 1972;12:59-129.
41. Stone HA, Leal LG. The effects of surfactants on drop deformation and breakup. *J Fluid Mech*. 1990;220:161-186.
42. Rednikov AY, Ryazantsev YS, Velarde MG. Drop motion with surfactant transfer in a homogeneous surrounding. *Phys Fluids*. 1994;6(2):451-468.
43. Li X, Pozrikidis C. The effect of surfactants on drop deformation and on the rheology of dilute emulsions in Stokes flow. *J Fluid Mech*. 1997;341:165-194.
44. Yuan Y, Li X, Tu J. Effects of spontaneous nanoparticle adsorption on the bubble–liquid and bubble–bubble interactions in multi-dispersed bubbly systems—a review. *Int J Heat Mass Transf*. 2018;120:552-567.
45. Jadhav SN, Ghosh U. Effect of surfactant on the settling of a drop towards a wall. *J Fluid Mech*. 2021;912:A4.
46. Liu AB, Mather D, Reitz RD. Modeling the effects of drop drag and breakup on fuel sprays. *SAE Trans*. 1993;83-95.
47. Hsiang LP, Faeth GM. Near-limit drop deformation and secondary breakup. *Int J Multiph Flow*. 1992;18(5):635-652.
48. Gunn R, Kinzer GD. The terminal velocity of fall for water droplets in stagnant air. *J At Sci*. 1949;6(4):243-248.
49. Best AC. Empirical formulae for the terminal velocity of water drops falling through the atmosphere. *Q J Roy Meteorol Soc*. 1950;76(329):302-311.
50. Zhao H, Liu HF, Xu JL, Li WF. Experimental study of drop size distribution in the bag breakup regime. *Ind Eng Chem Res*. 2011;50(16):9767-9773.

How to cite this article: Liu H-F, Wang Y-F, Zhao H, Li W-F, Xu J-L. Drop breakup and entrainment in the updraft. *AIChE J*. 2022;68(8):e17704. doi:10.1002/aic.17704